Methods in Oceanography 17 (2016) 264–281

Contents lists available at ScienceDirect

Methods in Oceanography

journal homepage: www.elsevier.com/locate/mio

Full length article

Evaluation of an acoustic remote sensing method for frontal-zone studies using double-diffusive instability microstructure data and density interface data from intrusions

Timothy F. Duda *, Andone C. Lavery, Cynthia J. Sellers

Applied Ocean Physics and Engineering Department, Woods Hole Oceanographic Institution, Woods Hole, MA 02543, USA

HIGHLIGHTS

- Measurements of double-diffusive instability ocean microstructure spectra made with sensors towed nearly horizontally.
- Demonstration of vertically thin intrusions stacked one above another.
- Predictive calculations of broadband acoustic backscatter strength from the measured instability microstructure.
- Prediction of backscatter from frontal intrusion density interfaces.
- One example backscatter prediction from field-measured microstructure is shown.

ARTICLE INFO

Article history:
Received 9 March 2016
Received in revised form
10 August 2016
Accepted 8 September 2016
Available online 19 October 2016

keywords:
Intrusions
Double-diffusive microstructure
Ocean mixing
Acoustic backscatter

ABSTRACT

Understanding intrusive exchange at oceanic water mass fronts may depend on building data-constrained models of the processes, but obtaining the needed representative and comprehensive data is challenging. Acoustic imaging (remote sensing) is an attractive method for mapping the three-dimensional intrusion geometry to enable the required focused in situ sampling of the mixing processes in intrusions. The method depends on backscatter of sound from sharp interfaces and from microstructure resulting from double-diffusive instability (DDI), a probable occurrence at intrusions. The potential of the method is evaluated using data collected using established methods in a field of intrusions south of New England. Above and beneath warm and salty

* Corresponding author.
E-mail address: tduda@whoi.edu (T.F. Duda).

http://dx.doi.org/10.1016/j.mio.2016.09.004

Echosounder
South New England shelf

intrusions may lie diffusive–convective DDI microstructure and salt-fingering microstructure, respectively, marking the intrusion boundaries, providing the backscattering features. The data show that both types of microstructure can occur in close proximity within intrusions, but the question of whether this is common or not is unanswered by the modest amount of data, as are questions about continuity of DDI-microstructure in intrusions (to facilitate intrusion acoustic imaging) and variability of DDI-driven heat, salt and buoyancy fluxes. Analysis here shows that detectable backscatter from DDI-microstructure will occur, and can be easily measured when plankton scattering is low enough. Interface scattering is also likely to be detectable. The DDI-linked microstructure data used here are inherently interesting in their own right and are presented in some detail.

1. Introduction

Intrusions are common features at ocean water mass boundaries and fronts. Efforts have been made to model intrusion dynamics and fluxes, for example by Walsh and Ruddick (1998) and May and Kelley (1997), but these require testing, and they also require input data because they rely on parameterized multi-modal diapycnal eddy diffusivities (salt-finger diffusivity, turbulence diffusivity, etc.) which require justification in the ocean and may depend on conditions surrounding the intrusion field. At this time, three-dimensional mapping and concurrent sampling of both finestructure and double-diffusive instability-triggered (DDI-triggered) microstructure within intrusions at lateral ocean water-mass boundaries (fronts), required for comprehensive validation of hypothesized intrusion-related fluxes, is a challenging measurement scenario. A particular challenge is the need to balance high resolution with broad coverage, a need that motivates a remote sensing strategy. Here, data from an intrusion are used to evaluate the strategy of using high-resolution broadband split-beam or multibeam echo sounders to map intrusions, allowing targeted in-situ sampling as well as a description of intrusion geometry.

To illustrate intrusive processes that might be investigated, data collected in a patch of dye tracer in an intentional injection experiment (Ledwell et al., 2004) shows that an intrusion can strain the patch (Fig. 1), intensifying diapycnal gradients faster than diapycnal mixing can destroy them. (This must be true over some time scale in some conditions, otherwise intrusions would not exist.) The figure shows structure in the y/ρ (north/density) plane on the eastern edge of a patch of dye in the third of five dye-dispersal experiments south of New England carried out in 1995–1997 (Ledwell et al., 2004). The depicted "boomerang" shape of the dye seen in the figure was unusual; virtually all transects showed dye areas of either oval shape or tilted oval shape (if shear was high), not the sideways-V deformation pattern that is suggestive of dye transport in an intrusion. Between the upper and lower edges of the patch was relatively fresh water apparently moving to the north. The 800-meter displacement to the north of the patch center, with respect to the upper and lower branches, is consistent with a steady advection speed of about 2.5 mm/s, impossible to instantaneously measure. (The actual flow may have been greater if the intrusive flow and the transect were not aligned.) Despite the challenges, definitive studies of frontal balances, diapycnal flux balances and processes, and advection in intrusions like this may be realizable with remote sensing mapping and informed in-situ sampling. In addition, extensive surveys could answer questions such as how variations of flow and stratification conditions at fronts can affect the intrusive processes.

The acoustic remote sensing strategy is examined here by calculating backscatter strength for DDI-triggered microstructure patches observed at the upper and lower boundaries of intrusions south of New England with a towed system. The work shows that the possibility of acoustic backscatter

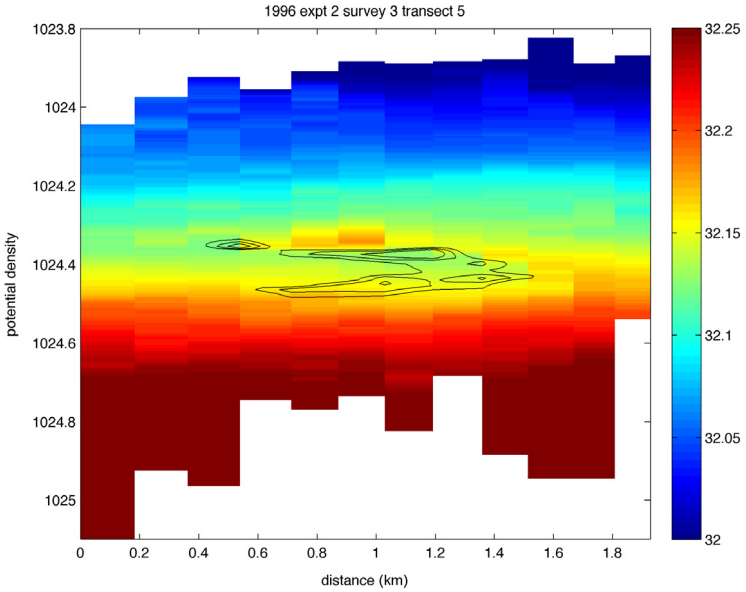

Fig. 1. Salinity in a dye experiment tow-yo transect four days after concentrated dye injection is shown in color, as a function of south/north distance and potential density. The black contours are of fluorescein dye concentration. The upper and lower legs of the patch at 0.8 km are 4 m apart in the vertical. The dye patch was getting pulled apart in the isopycnal direction fast enough that diapycnal mixing had not erased the strengthening diapycnal gradients. (For interpretation of the references to color in this figure legend, the reader is referred to the web version of this article.)

intrusion mapping exists, as determined using a proven model of volume scattering (Lavery et al., 2003, 2010) and a simple model of interface scattering, with the caveat that other scatterers in the ocean may mask the signals, if present.

Details of the intrusion and microstructure data are presented for comparison with other published observations of this type (Gregg, 1975; Gargett and Schmitt, 1982; Marmorino, 1987; Osborn, 1988). These data demonstrate that the DDI patches in the New England area intrusions can have a high aspect ratio (tens of meters or more across, one meter tall) that may foster acoustical detectability with a mobile system (i.e. not missed with intermittent pings, trackable over space and time). A high aspect ratio of DDI microstructure patches along intrusions has been found once before using a US Navy submarine near San Diego (Osborn, 1988). The amount of information in these microstructure data suggest an ability to quantify DDI mixing activity and intrusion evolution with in situ towed, AUV or glider surveys guided by remote sensing.

An additional rationale for presenting the data is to document the well-known challenges of in situ investigations of intrusion dynamics and cross-frontal exchange, particularly when double-diffusive instability fluxes play a meaningful role. Such fluxes can be estimated using laws (parameterizations) that depend on the details of the stratification that are challenging to resolve, and are challenging to sample effectively throughout the lifetime of a particular intrusion. Acoustic mapping might aid the intrusion process studies. The flux estimates, along with broad scale environmental information, could for example be used to build a new empirical or heuristic model of intrusive exchange, or to validate a theoretically based model such as Walsh and Ruddick (1998). Many of the steps in this model building and validation process continue to be very challenging.

The paper presents details of the measurement system and the location of microstructure data collection in Section 2. Section 3 presents aspects of intrusion geometry. Section 4 presents details of the double-diffusive microstructure signatures found in the data. (Acousticians and remote-sensing technologists may choose to skim through or skip Sections 2–4.) Section 5 presents calculations of expected acoustic backscatter from microstructure of the observed type and from interfaces, with

implications for remote sensing of intrusion double-diffusive mixing activity. Section 6 concludes. An Appendix presents details of the backscatter cross-section calculation.

2. Measurement system, data processing, and geographic location

2.1. Measurement system

The data shown here are byproducts of a modest field effort in August 2004 south of New England that had the goal of studying shear-driven mixing away from intrusions. The effort is documented in a report (Duda and Sellers, 2016). The relatively inexpensive towed system that was used was built at WHOI to record detailed water column measurements while underway. The system and its performance are documented in a paper (Rehmann and Duda, 2000), but some details are reproduced here for completeness, and new information is added. The towed package (sensor platform) has a cage with a stabilizing tail, is typically towed from the rear of a research vessel (although pitch would be reduced if towed from a boom amidships), and the depth is controlled by the winch spool payout. The sensor platform was towed from the stern of the ship at about 4 to 4.6 knots (2–2.3 m/s) with variable vertical profiling rates, including zero (horizontal tows). For tracer sampling studies the system is referred to as Tracer Sampling Sled (TSS) or Dye Sampling System (DSS) (Ledwell et al., 2004). With microstructure sensors it is referred to as MicroTow (MT). The platform, in a configuration without microstructure sensing, was also used in a successful study of dissipation in gigantic internal waves in the South China Sea (Orr and Mignerey, 2003).

The platform had a Seabird Electronics Model 9+ CTD aboard, with two separate (redundant) pumped temperature/conductivity cell systems. These measured at 24 Hz and were averaged and recorded at 12 Hz, double the recording rate of pre-2004 deployments. A Seabird Electronics "deck-unit" board-set was in the platform, converting the data and forwarding via serial port to the data-acquisition computer (DAC). Platform pitch, roll and heading (yaw) data from the TCM2 magneto-inductive sensor were recorded at 7 Hz by the DAC. Microscale signals were sensed with two 2-electrode (dual needle) Seabird Model SBE7 conductivity probes sampling at 400 Hz (200 points per meter, typically), specially ordered to pass high-frequency signals but having standard pre-emphasis. (2-electrode probes are known to not maintain calibration.) The sensor signals were passed through a differential amplifier, a monolithic 4-pole Butterworth low-pass filter with a 120-Hz cutoff frequency, then sampled by an analog to digital converter in the DAC. The SBE7 output signal with the probe in air (zero conductivity signal) was 2.7 mV rms, setting the system noise level at thermal variance dissipation rate $\chi_T = 2 \times 10^{-10}$ K^2 s^{-1} in water of uniform salinity.

The 9+ and SBE7 probes were arranged horizontally across the nose of the platform to all sample at the same depth (Fig. 2). Below them a two-axis electromagnetic current meter was mounted to measure the flow speed past the probes and the angle of attack of the platform, with data collected by the 9+ CTD. Data from all sensors were collected by the DAC, packaged into blocks, and transmitted to the ship via RS485 serial link through two conductors of the ∼600-m long 0.322-inch diameter armored electromechanical cable. DC power for the system was delivered via the third conductor (feed) and the cable armor (return). Redundant topside data collection computers provided visualization of the data streams and stored the data on disk every ten minutes.

2.2. Data processing

The finestructure (12-Hz) data were processed following Rehmann and Duda (2000) and Duda and Rehmann (2002), with some additional processing, as explained below. The pressure signal from the Seabird system is noisy, so it was low-pass filtered such that the output time series has the undulating quality one would expect from a towed platform. Next, gradients for temperature T, salinity S, density ρ and depth z (approximated using pressure p) were computed for 2-s blocks of the 12 Hz data. These are dT/dz, dS/dz, dS/dT and $d\rho/dz$, buoyancy frequency squared N^2, and density ratio $R_\rho = \alpha dT/dz(\beta dS/dz)^{-1}$. Data blocks with poorly-fitting dT/dz and dS/dz regressions ($R^2 < 0.5$) are not used for any physical oceanographic investigations involving quantitative finestructure. The angle

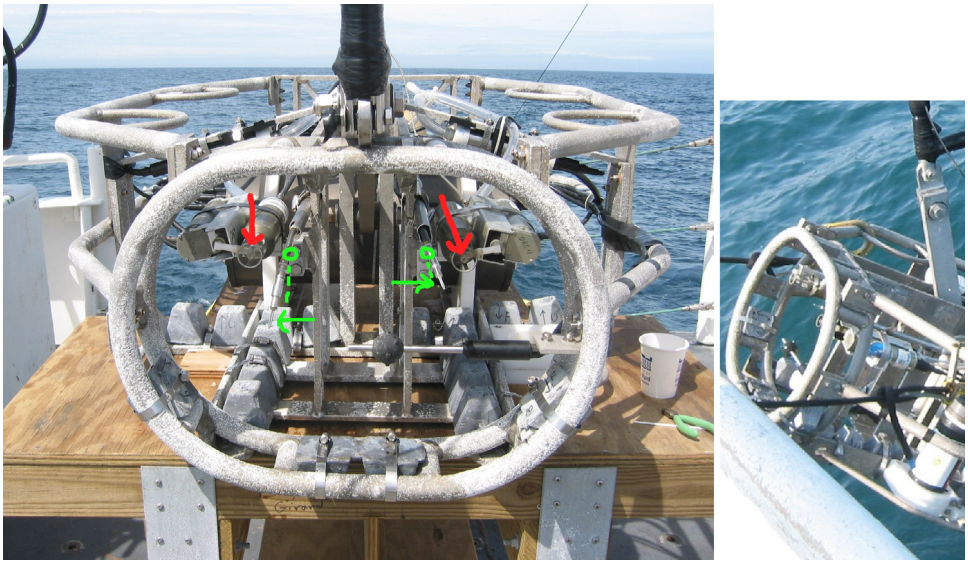

Fig. 2. (left) This photo of the sensor platform shows probe positions across the top of the front opening. From left: one CTD probe pair (vertical arrows point to CTD probe inlets), two 400-Hz dual-needle conductivity probes pulled outward for submersion cleaning (green o's show approximate mounted locations, horizontal arrows indicate the probes), and another CTD probe pair. The central black ball is the two-axis current sensor. (right) Here, the dual-needle probes are in sampling position. (For interpretation of the references to color in this figure legend, the reader is referred to the web version of this article.)

of attack of the sensors is computed using the forward and vertical components of nose current and microstructure data without a usable low angle of attack (between −20 and 20 degrees) are flagged for deletion from microstructure analyses. The thermal and haline expansion coefficients α and β are computed for the same blocks, and the density ratio R_ρ is then computed (Schmitt, 1994), along with the Turner angle (Ruddick, 1983). The processing added for this work is the computation of potential temperature θ and potential density σ_θ (reference pressure 0 dbar), averages of θ, S and σ_θ within σ_θ bins of width 0.01 kg m^{-3}, and spiciness $\pi(\theta, S)$ (Flament, 2002) for the bin-averaged θ and S, and the second derivative of π with respect to σ_θ, $\pi_{\sigma\sigma}(\sigma_\theta)$. The second-derivative quantity has been demonstrated to be useful for locating intrusions, having extrema in intrusions (Shcherbina et al., 2009).

The microstructure data were also processed as in Rehmann and Duda (2000). The 400-Hz conductivity timeseries were computed by filtering to remove the preemphasis and applying a calibration algorithm. The conductivity gradient spectrum was computed for 1-s blocks using a periodogram method, with wavenumbers k computed from temporal angular frequencies ω using the 1-s averaged flow speed U past the sensors, $k = \omega/U$. The upper-bound and lower-bound estimated thermal variance dissipation rates χ_{hi} and χ_{lo} were computed in the same blocks using methods of Washburn et al. (1996) that utilize the finescale gradients, as explained in detail for this system by Rehmann and Duda (2000). Basically, the temperature gradient spectrum is estimated from the measured conductivity gradient spectrum, and is then integrated and multiplied by the heat diffusion coefficient and the isotropy factor 3 to form χ_T. Depending on local T or S vertical gradients, either χ_{hi} or χ_{lo} will be a better choice to represent χ_T. To directly compare finescale and microstructure data, a 1.0 s delay was applied to the microstructure data. This step was implemented after noting a timing discrepancy between 400-Hz and 12-Hz conductivity patterns. The one-second latency of the 12-Hz data is apparently introduced by the Seabird "deck unit" prior to recording by the DAC. Vibrations of the probe do not create troublesome false signals (noise) in the conductivity microstructure data for reasons explained by Rehmann and Duda (2000), although signals present at the smallest resolved scales may be distorted by intense vibration. The vibration tolerance of moving scalar probes is also demonstrated by the data in Gregg (1975). Finally the conductivity probe has a slight roll off at resolved wavenumbers between 30 and 100 cycles per meter (Meagher et al., 1982;

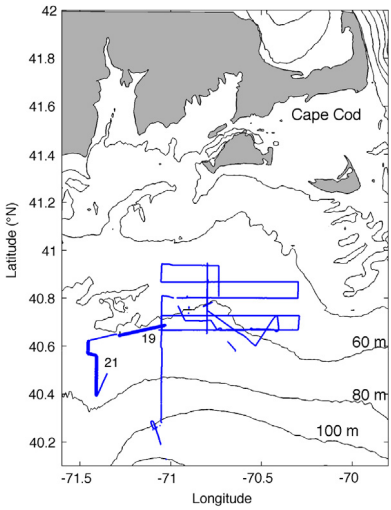

Fig. 3. The tow tracks for the entire program are plotted. The transects mainly analyzed here (19 and 21) are plotted with thicker lines. The tow directions are west-southwest and south, respectively.

Hill and Woods, 1988) that does not substantially affect the variance-containing portion of spectra in DDI-based microstructure, and influences dissipation estimates less than errors introduced when estimating χ_T from conductivity measurements.

2.3. Location

The location of data collection is shown in Fig. 3. The system was towed for 25 transects of varying lengths, almost entirely in tow-yo mode, with easily identifiable intrusions in many of the approximately 700 individual profiles. The report provides further information about the water masses and intrusions in the area, although the transects were too sparse to map these in detail (Duda and Sellers, 2016). The data from transect 19 show very clear double-diffusive instability signatures on the 14th profile (7th upward profile, called t19:p14). These data are shown in detail in Section 4 and were chosen for analysis of acoustic scattering cross section (Section 5).

3. Intrusion height and spacing

Intrusions are pervasive in the sampled area. They are closely spaced in the vertical, as was observed by Gregg (1975) near San Diego. The close spacing has not been well documented for this location, and was not mentioned in an intrusion study by Lentz (2003). Fig. 4 shows the temperature, salinity and density from transect 19. An intrusion within profile 14, examined in detail later, is at the lower extreme of the measurements at kilometer 6.3. Warm salty intrusions appear as peaks of salinity as a function of depth, often stacked vertically one above another, primarily in the saltier measured regions.

More extreme vertical layering is seen in transect 21. Finestructure and microstructure data from upward profile tr21:pr37 are plotted in Fig. 5. The T and S profiles suggest five warm salty intrusions, some spaced only a few meters apart in the vertical. These are thinner in vertical scale than is suggested by the tabulations of intrusion thickness published by Lentz (2003), who was not analyzing data meant to resolve high-wavenumber features. Five warm salty features (peaks of spiciness) are located at 49 dbar (8.4 °C), 46.5 dbar (8.7 °C), 43 dbar (8.8 °C), 37 dbar (9.3 °C), and 34 dbar (10.3 °C). The five peaks in spiciness (warm and salty water) are visible in the density-bin-averaged θ, S diagram, with the extrema of the spiciness 2nd derivative $\pi_{\sigma\sigma}\ (\sigma_\theta)$ marking intrusions as explained by Shcherbina et al. (2009). For this profile $\pi\ (\sigma_\theta)$ is nearly oscillatory so both its first and

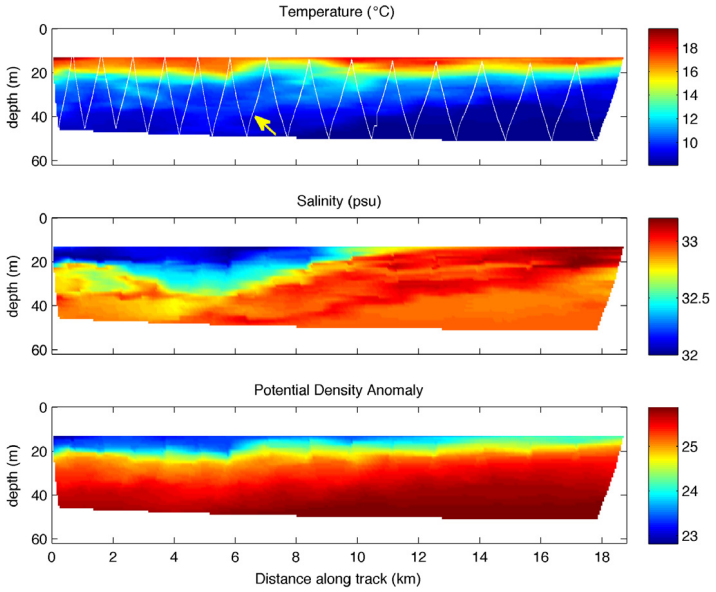

Fig. 4. The temperature (top), salinity (center) and potential density anomaly (σ_θ) (bottom) are shown for transect 19. The distance plotted here is computed by integrating the forward component of the velocity sensor on the platform and is less than the track length (21.8 km) due to currents or minor flow distortion. The platform trajectory (left to right) is shown with a white line in the temperature panel. Profile 14 (upward) is indicated with the arrow in the top panel.

second derivatives are good indicators of intrusions. Analysis of the 2nd derivative $\pi_{\sigma\sigma}(\sigma_\theta)$ shows evidence of intrusions for the majority of the data set.

4. Double-diffusive instability signatures, properties, and fluxes

The warm salty intrusions can be propelled by fluxes from salt-finger instability on their lower sides and from diffusive–convective (diffusive layering) instability on the upper side (Turner, 1973; Schmitt, 1994). The near-horizontal paths of the towed probes facilitate the interpretation of the structures as the product of double-diffusive instability for two reasons: the horizontal microscale features are directly measured in the manner of Gargett and Schmitt (1982) and predecessors, and the stratification is measured at the vertical scale of a centimeter. Comparable towed or AUV/glider (quasi-horizontal path) ocean microstructure measurements have been made in the past (Gargett and Schmitt, 1982; Washburn and Gibson, 1982; Washburn and Deaton, 1986; Rehmann and Duda, 2000; Osborn and Lueck, 1985; Fer et al., 2014, and others), but only a few data sets are available showing double-diffusive instability features in vertically stacked intrusions in a dynamic coastal environment (Gregg, 1975; Osborn, 1988).

Finestructure and microstructure data from upward profile t19:p14 are plotted in Fig. 6. Three features exhibiting salinity and temperature increases with depth can be seen, at 28.5, 36, and 46 dbar. The deeper two are intrusions, with this interpretation supported by the salinity reductions beneath the salinity maxima, with temperature maxima also occurring. The left three panels plot data versus pressure, the others plot data versus time. The 4th panel from the left shows the 12-Hz conductivity in black and the 400-Hz conductivity in blue (with poor absolute calibration adjusted for plotting), verifying the alignment of the two data streams.

Fig. 7 is an expanded view of a portion of the Fig. 6 data, centering on the DDI activity above and below the intrusion centered at 47 dbar. There are several things to note in the figure:

(1) The location of peak temperature in the intrusion is 0.2 dbar shallower than the peak salinity location. (Details of the plotted salinity and density are not influenced by adjustments to the

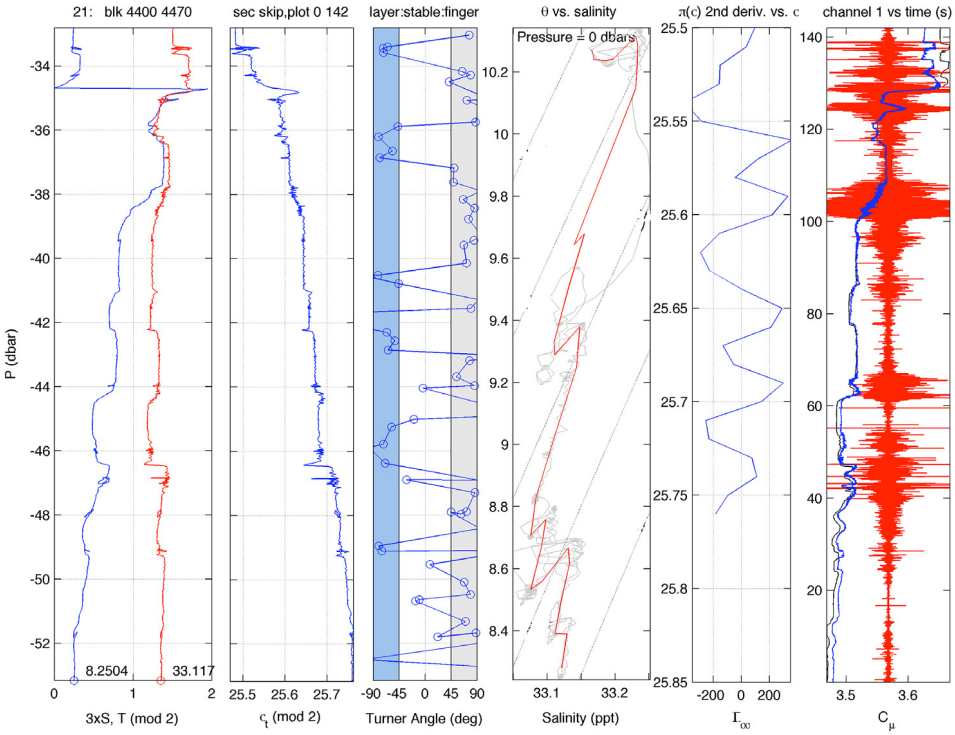

Fig. 5. From the left, the first panel shows, modulo 2, temperature T and salinity S in profile tr21:pr37 (upward) versus pressure. The T and S values in the first point are listed. The 2nd panel shows density anomaly (σ_θ) and the 3rd panel shows the Turner angle, each also versus pressure. The fourth panel is a θ, S plot, with 12-Hz data shown in gray and 0.01 width density bin averages in red, following Shcherbina et al. (2009). The fifth panel shows $\pi_{\sigma\sigma}$ versus potential density. The final panel shows the 12-Hz (black line) and 400-Hz conductivity (blue line, with arbitrary offset) and the first difference of the 400-Hz signal (red). (For interpretation of the references to color in this figure legend, the reader is referred to the web version of this article.)

conductivity cell thermal lag correction algorithm for these near-horizontal tows through these waters with small temperature changes, see Ledwell et al. (2004).)

(2) The Turner angle is in the diffusive–convective instability range [−90°, −45°] above the intrusion, and typically in the salt-finger range [45°, 90°] below it.

(3) The 400-Hz conductivity trace shows stair-steps above the intrusion, consistent with diffusive–convective staircases. The two-second time interval for the layers (the time-lag between interfaces) corresponds to a layer height of approximately 27 cm, and a horizontal probe displacement of four m along the diagonal path (2 m s^{-1} times 2 s).

(4) The vertical density gradients are variable above and below the intrusion with an average value of $N^2 = 4 \times 10^{-4}$ rad^2 s^{-2} (11.4 cph).

(5) Thermal variance dissipation rates (χ_T values) range from 10^{-8} K^2 s^{-1} (the at-sea noise level) in the intrusion core to 10^{-5} K^2 s^{-1} in the active region.

Fig. 8 shows spectra from the microstructure patches. The peak wavelength of the finger-zone spectrum is 5 cm, near the wavelength of fastest growth of 3.3 cm, for density ratio of 1.3, calculated using methods of Schmitt (1983), and in the finger (cell) size range reported by Osborn (1988). Five cm is also the observed peak wavelength for the DDI diffusive–convective microstructure spectra, far smaller than the ∼30 cm heights of the individual convecting layers visible in the 400-Hz conductivity data (Fig. 7, panel 4, blue, 45.5 to 46.5 dbar zone).

The t19:p14 intrusion at 47 dbar depicts DDI in action with remarkably clarity, but the DDI signatures on adjacent upward profiles 12 and 16 are not as clear (Fig. 9), and the intrusion itself had

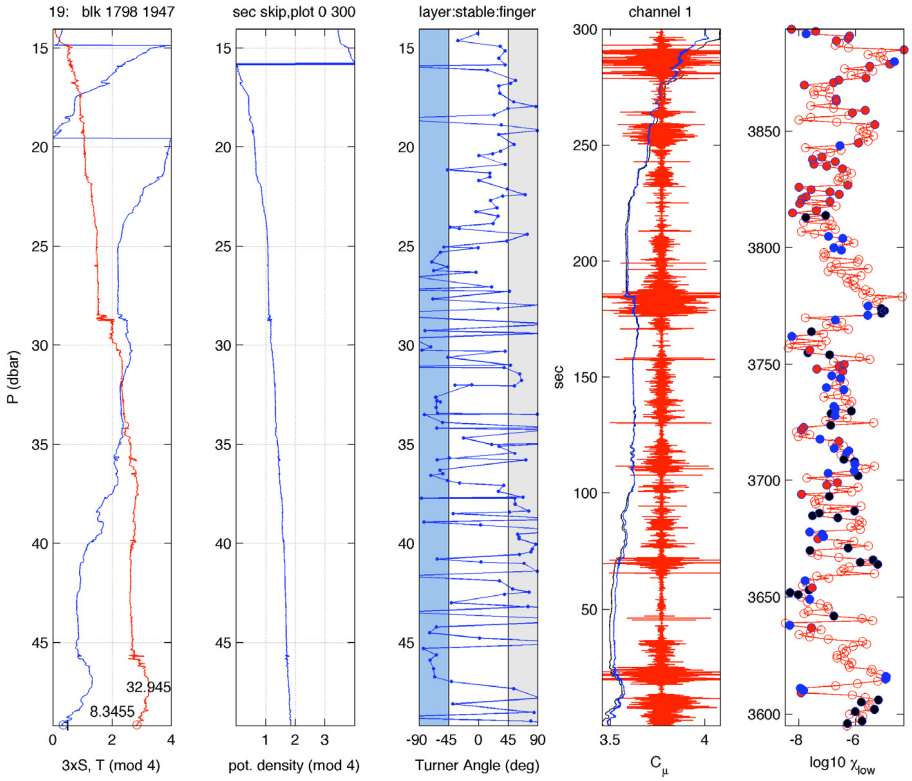

Fig. 6. Finestructure and microstructure data from profile t19:p14 (upgoing) are shown. Panel 1 (left) shows, versus pressure, temperature (blue) and salinity times 3 (red), modulo 4. Temperature and salinity values at the lower end are printed. The next panel shows potential density, also mod 4. Panel 3 shows the Turner angle computed for 2-s data blocks. Panel 4 shows 12-Hz (black) and 400-Hz conductivity (the 400-Hz trace has been adjusted by a constant to match), and the gradient of 400-Hz conductivity (red), all versus time. Panel 5 shows the lower-bound of computed thermal variance dissipation rate, with color codes indication stratification type: strongly DDI finger-favorable (black), strongly DDI layer-favorable (blue), doubly-stable (red), see panel 3. Time in panel 5 is seconds from start of record. (The automated classification is only a guideline.) (For interpretation of the references to color in this figure legend, the reader is referred to the web version of this article.)

different structures in each sensor transit (if indeed the sensors passed through it). This exemplifies the sampling difficulty. The temperature peak of the intrusion at 47 dbar is only present in one profile, with the others at 600 s lag (∼1200 m away) showing entirely different structure. The concurrent existence of DDI diffusive–convective and DDI fingering was not unique to t19:p14, but it was rare. Of order 700 profiles collected, fewer than 15 show this behavior.

The eddy diffusion coefficients in the three types of stratification were computed using the Osborn–Cox model as outlined in a report (Duda and Sellers, 2016). The mean heat diffusivities are $K = 6.2 \times 10^{-7}$ m^2/s for doubly stable conditions, 1.2×10^{-6} for waters having salt-finger DDI conditions, and 5.2×10^{-6} for waters having diffusive–convective DDI conditions. (Means are of Osborn–Cox model diffusivities computed as a function of N in 6 N-bins per transect, with equal quantity of data in each bin. The procedures, and complete doubly stable regime results, can be found in the report. Confidence intervals (95%) from natural data spread are about ±10%; uncertainties from potential violation of the Osborn–Cox model assumptions are not quantifiable and are probably larger.) For comparison, other reported diffusivities for this area are (1) 0.5 to 9×10^{-6} m^2/s, obtained from five dye-dispersal studies (Ledwell et al., 2004, see Fig. 1); (2) 0.6 to 3×10^{-5} m^2/s, effective diffusivities acting in layered structures (Duda and Rehmann, 2002); (3) 0.2 to 1.3×10^{-5} m^2/s from microstructure profiling (Oakey and Greenan, 2004); (4) 0.5 to 2×10^{-5} m^2/s from microstructure profiling (MacKinnon and Gregg, 2003).

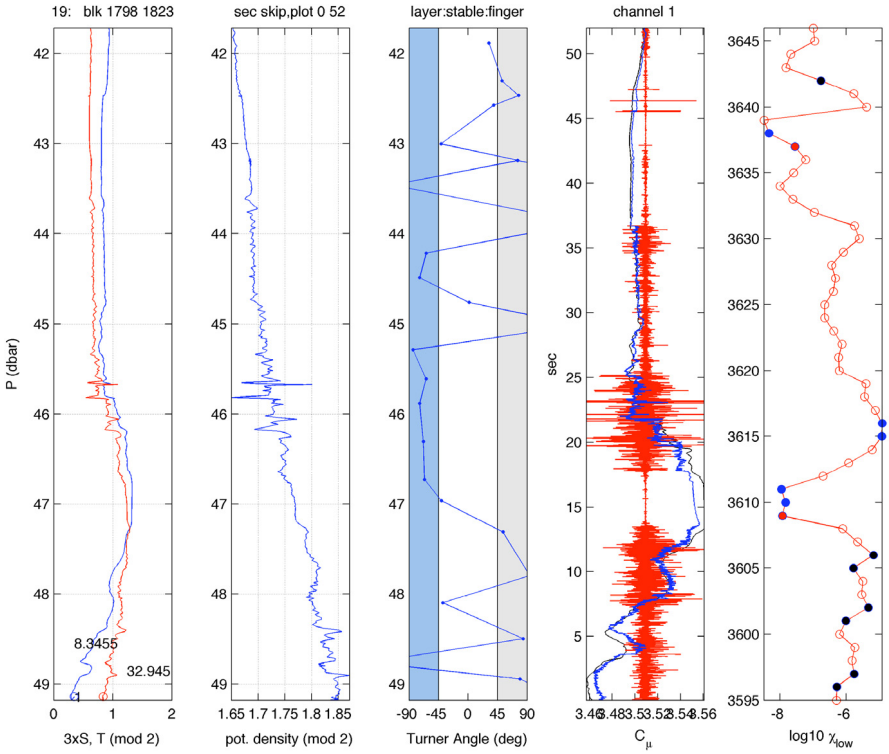

Fig. 7. Fifty-two seconds of data from profile t19:p14 that appear in Fig. 6 are plotted with expanded scales. The intrusion at 47 dbar is evident. The apparent diffusive–convective microstructure above the intrusion core is separated from the apparent salt-finger microstructure below it by an area of virtually no microstructure (laminar flow). The probe rise rate is 0.135 m/s for this section of tow (3 points per mm at 400 Hz.) The high dissipation signal near 42.5 decibars (seconds 46 and 3640 in the right two panels with vertical time axes) is an artifact that can be classified by a high value of 400-Hz time series kurtosis (not shown). (For interpretation of the references to color in this figure legend, the reader is referred to the web version of this article.)

The fact that the diffusive–convective DDI value is highest would suggest that the fluxes on the upper side of the intrusions would dominate total diapycnal flux in the area (these are not sites of low diapycnal gradients that would counterbalance high K to reduce flux). The median heat flux for diffusive–convective DDI waters was 7.5 W/m^2, with diagnosed fluxes (mean of K times local dT/dz) computed in 2-s data windows. The trimmed-mean results, with 5% or 10% of the outlier values removed, were 25 and 19 W/m^2, respectively. These are larger than other values of 1 to 4 W/m^2 reported for these waters (Oakey and Greenan, 2004). Data from the salt-finger DDI regime are probably the worst of these for using high-rate conductivity sensing to evaluate χ_T and then using the Osborn–Cox model to quantify eddy diffusivity and flux. This is because molecular heat fluxes initiate the finger motions, strengthening salinity anomalies with respect to temperature anomalies, adding uncertainty to χ_T estimation. This does not occur in the doubly-stable regime, where T and S structure is generated equally by strain, nor in the diffusive–convective DDI regime where molecular-diffusive interfacial heat flux creates thermally buoyant plumes.

Tabulating the salt, heat and buoyancy fluxes in all measured patches of DDI activity is beyond the scope of this paper. However, fluxes are estimated for the t19:p14 interfaces above and below the salty intrusion (Fig. 7), using established interfacial flux methods. Fig. 10 shows that the upper-side "interface" is actually composed of three interfaces, each below a convecting layer. Heat flux at these interfaces can be estimated using the 4/3-power flux-law formula of Kelley (1990) as rewritten in a more recent paper (Timmermans et al., 2008, Eq. (6)) with the result $F_H = 2.2 \times 10^{-6}$ °K m s^{-1}.

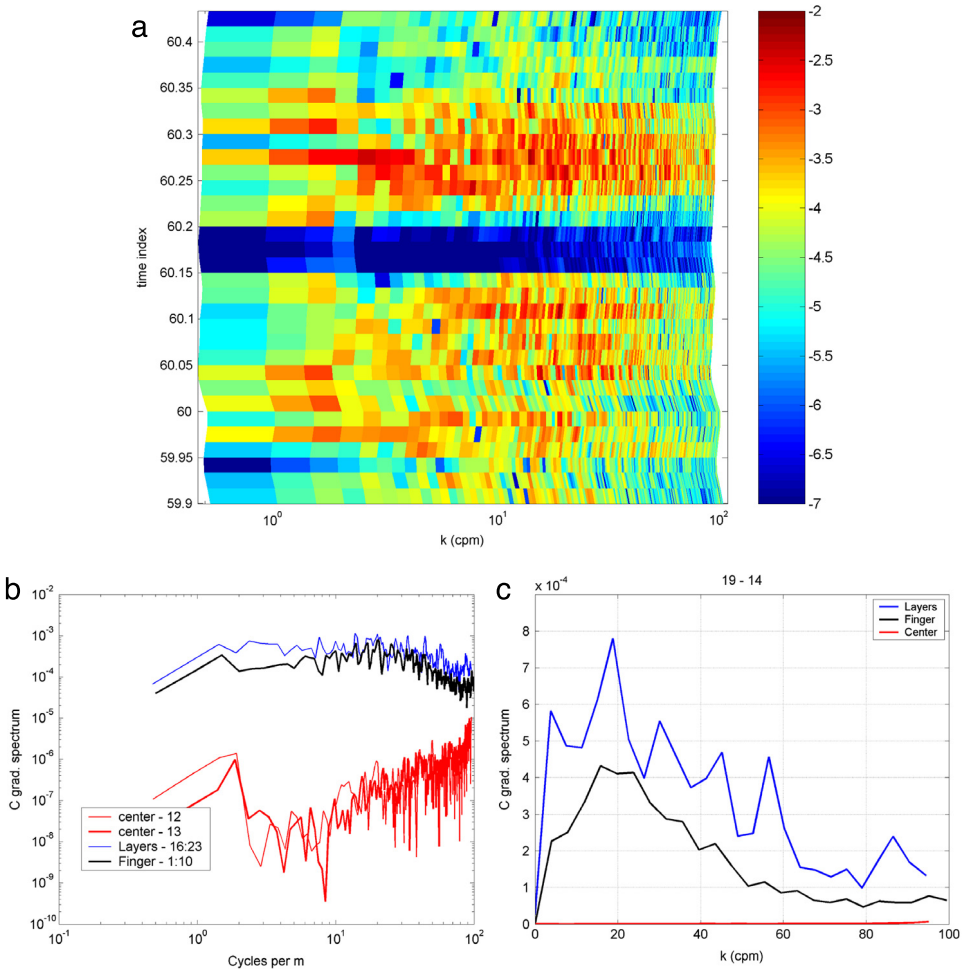

Fig. 8. (a) Conductivity gradient spectra from the featured intrusion of Fig. 7, computed once per second, are plotted in color. Units are $(S/m^2)^2$ per cycle/meter. The time index is in minutes since the transect start; the time period is seconds 0–29 of panel 4 of Fig. 7, seconds 3595–3625 of panel 5. (b) Plotted are average spectra from the finger-prone (earlier, deeper) portion of the record (black line), the diffusive/convective instability (later, shallower) portion of the record (blue line), and the core of the intrusion (center, red lines). (c) The spectra of (b) are shown in linear form. The linear plot shows that the variance of the diffusive/convective microstructure is double that of the fingers, and that most of the variance occurs between 5 and 50 cpm. (For interpretation of the references to color in this figure legend, the reader is referred to the web version of this article.)

(This is heat flux $\rho c_p F_H$ of 9 W m^{-2}, 30–180 times higher than Timmermans et al. (2008) reported for diffusive–convective staircases in the Arctic; c_p is heat capacity.) The buoyancy flux enumeration of the heat flux is $\alpha F_H = 3.2 \times 10^{-10}$ m s^{-1} (out of intrusion). Key parameters used in the calculations are $R_\rho = 0.7$ and interface step $\Delta T = 0.4/3$, deducible from Figs. 7 and 10 (note that the Timmermans et al. and Kelley papers, and some others, use an R_ρ definition inverse to ours). The salt buoyancy flux can be estimated using the flux ratio (Kelley, 1990), and is 1.2×10^{-10} m s^{-1} (buoyancy flux into intrusion), with the *net outward computed upper-side buoyancy flux* of 2×10^{-10} m s^{-1}. Flux at DDI finger zones below the intrusion can be estimated with Stern's formula, as adjusted by Schmitt and Evans (1978), with the required parameter $\Delta S = 0.1$, yielding salt buoyancy flux $\beta F_S = 3.5 \times 10^{-9}$ m s^{-1} (into the intrusion), greater than on the upper side, and a counterbalancing thermal buoyancy flux of 3.2×10^{-9} m s^{-1} (out of the intrusion, computed using buoyancy flux ratio

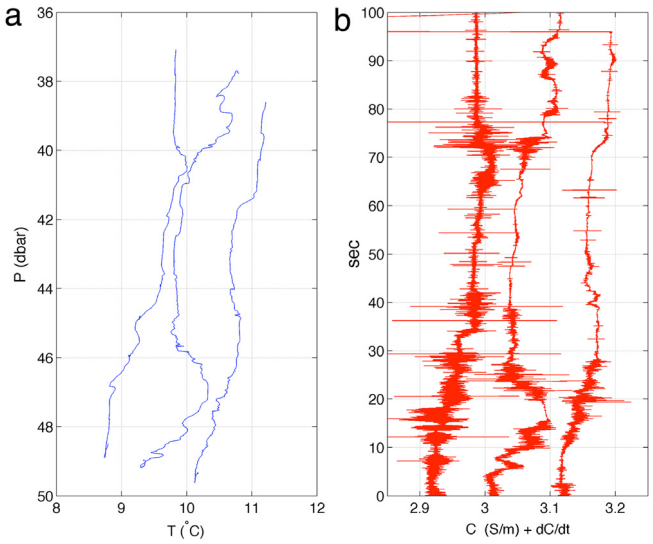

Fig. 9. (a) The temperature (T) on three consecutive upward profiles is shown. The middle one is profile t19:p14 seen in Figs. 5 and 6. Profile t19:p12 T is the left, t19:p14 T is in the center offset by one degree, and t19:p16 T is at the right offset by two degrees. (b) The sum of 400-Hz conductivity and the down-scaled derivative of this is plotted, offset by 0.12 S/m units from one another, and with time used as the ordinate. Profile 12 shows DDI fingering deeper than 44 dbar, and profile 16 shows DDI fingering deeper than 46 dbar.

0.91 Turner, 1973, equal to a whopping 87 W m^{-2}), resulting in a *net inward flux* of 3.1×10^{-10} m s^{-1}. The estimated net inward finger buoyancy flux is the dominant term by a slight amount, suggesting intrusion density decreasing with time. Uncertainties in the flux estimates stem from assumptions made in the theory and in the interpretations used to quantify ΔT and ΔS (possibly $\pm 20\%$).

These provocative numbers cannot be considered to be representative of all intrusions, and provide further motivation to guide more definitive intrusion studies with remote sensing mapping methods. However, the flux estimates show the same sense of density evolution as depicted in Figs. 1–3 of the intrusion modeling paper of Li and McDougall (2015), so the data support the ideas in that paper. Note that the higher flux estimates for the finger regime, among these two flux quantifications, are not trivially compatible with the higher diffusivity estimates for diffusive–convective conditions than for salt-finger conditions, but they are not inconsistent.

5. Acoustic remote sensing analysis for intrusions

Testing the validity of intrusion models where DDI activity is key, such as Walsh and Ruddick (1998) or May and Kelley (1997), require measurement of DDI-driven fluxes and intrusion geometry in three dimensions. The first of these, measuring fluxes at the tops and bottom of intrusions, is shown to be possible in Section 4 but sustained sampling of these fluxes and of the evolving intrusion finestructure characteristics require the intrusions to be located and measured across a front, as done by Shcherbina et al. (2010) with a towed package. Once again we emphasize that an acoustic remote sensing "vertical curtain" view of water mass interfacial structure can facilitate such data collection.

The microstructure data presented in Section 4 are adequate to assess the expected acoustic backscatter return from DDI microstructure patches. The expected echo strength from a volume filled with microstructure can be estimated directly from the spectra of temperature and salinity fluctuations; this is done here. The return from flat interfaces associated with diffusive–convective activity is also computed for comparison.

The value and power of new broadband acoustic backscatter remote sensing and survey systems and methods have been demonstrated, for example by Lavery et al. (2010). Typically plankton and

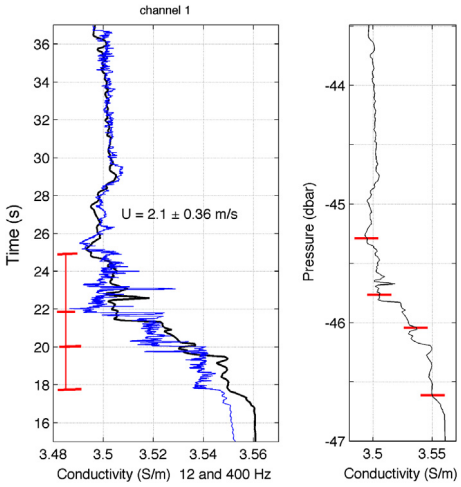

Fig. 10. Data from t19:p14 are shown in detail. (left) The 12-Hz conductivity is shown as a thick line, and the (offset, uncalibrated) 400-Hz conductivity as a thin line, both plotted vs. time. Three convective layers can be seen, in effect a short diffusive–convective staircase, with interfaces delineated by short horizontal on the left. (right) The 12-Hz conductivity is replotted versus filtered (de-noised) pressure, with the delineating markers drawn to show the layer heights of at most 0.55 m.

shear-instability type turbulence is detected and examined. Single narrowband systems have proven useful in the past, but there are advantages to collecting data over a broad range of frequencies, and using individual channels that use broadband signals. For example, ocean microstructure and zooplankton have backscattering efficiencies that have different frequency dependence, allowing them to be differentiated in echograms. This motivates the question of whether modern systems can detect and differentiate DDI diffusive-convection and DDI fingering activity in a field of intrusions (see Fig. 5), allowing both the geometry and the processes at work to be detected.

Most ideally the acoustic data would provide all necessary data in stand-alone fashion, but it is more realistic to expect the backscatter data would need augmentation by dropped, towed, or autonomous moving sensors strategically placed using the acoustic mapping. Acoustic backscatter data can provide quantitative information about turbulence and turbulent flux (Lavery et al., 2013), but this capability diminishes with decreasing signal to noise ratio, which is often low for ocean microstructure (Lavery et al., 2010).

5.1. Volumetric microstructure scattering

The data shown in Figs. 7 and 8 can be used to test whether the expected acoustic signals are adequate to detect and differentiate DDI-diffusive–convective and DDI-finger activity. The volume scattering coefficients (σ_v) for both the DDI-DC and DDI-finger microstructure are computed using the model of Lavery et al. (2003). Fig. 11 presents the volume scattering strength $S_v = 10\log_{10}(\sigma_v)$, across a 400-kHz frequency band for a vertical-beam monostatic geometry. The computation method is explained in the Appendix. The inputs used for the calculations are the observed conductivity gradient spectra (Fig. 8). The depicted data are very well suited to this computation because 8 or more seconds of data were collected in each microstructure patch, covering 16 or more meters of distance, allowing good spectral estimation. Other parameters that are required are listed in Table 1, some of which will strongly vary from one intrusion to another, and others that do not. The figure shows that DDI-DC and DDI-finger echoes cannot be differentiated by spectral shape.

The diffusive–convective returns are expected to be larger than the fingering returns by 2–4 dB. Both are much less than the −55 dB level for active upper ocean turbulence (estimated using dissipation data from MacKinnon and Gregg, 2003), but detectable. Oceanic echoes from zooplankton

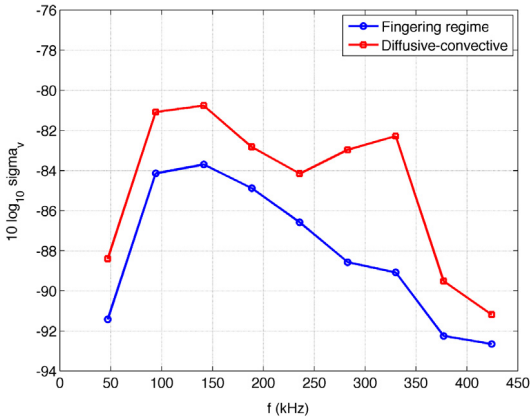

Fig. 11. The predictions for volume scattering strength for the fingering and diffusive–convective type microstructure patches of Figs. 7 and 8 are shown in dB. Fingering structure gives slightly lower values. These are 25–32 dB less than scattering from ocean turbulent microstructure with high dissipation, Lavery et al. (2010).

Table 1
Parameters used in the computation of the scattering cross-section σ_v.

Parameter	Symbol	Value
T dependence of conductivity	A	2.42×10^{-2}
S dependence of conductivity	B	2.55×10^{-2}
Linearized background dS/dT ($R_\rho = \pm 0.8$)[a]	m	0.25
Fractional sound speed dependence on T	a	3.55×10^{-3}
Fractional sound speed dependence on S	b	1.24×10^{-3}
Reference sound speed (m/s)	c_0	1500
TS correlation correction factor, conductivity gradient spectrum to T grad. spec. conversion	s	0.4
Thermal expansion coefficient	α	0.15×10^{-3}
Haline contraction coefficient	β	0.76×10^{-3}

[a] Indicates that the parameter will strongly vary in time and space.

measured with a broadband system in SW06 were typically greater than these levels (Lavery et al., 2010), but many data from ship-board echo sounders show maximum returns below −85 dB, so the DDI microstructure should be detectable. The finding is that the usefulness of acoustic remote sensing of DDI microstructure to map intrusions and to guide additional sampling would depend on operating in a study area or season with a suitably low concentration of zooplankton.

Fig. 12 shows volume scattering strength data collected with a Simrad 38-kHz split-beam scientific echo sounder during *RV Neil Armstrong* Scientific Verification Cruise 6 at an area just south of this data collection region. Transceivers operating at 18, 38, 70, 120 and 200 kHz, were used, each capable of broadband and narrowband operation. The figure shows scattering at interfaces associated with intrusions, verified with CTD data, in the range of −75 dB volume scattering strength. The two flat blue layers seen at the right of the zoom box are the top and bottom of a warm salty intrusion. Above and below the intrusion there is intermittent backscatter in the −80 dB range from structure that would be consistent with salt fingers (below) and diffusive–convective eddies (above). This example shows that interfaces at intrusions may be at least as visible in the ocean as the DDI microstructure. Scattering from interfaces is considered in the next section. Many hours of data such as these showing probable (and in some cases CTD verified) intrusion scattering were collected during the cruise, with signatures seen at all frequencies.

Fig. 12 is worthy of a few more comments. Because the system was changed from broadband to narrowband mode during the depicted time period, the difference in resolution of the two

modes is clear to see. The individual scatterers (fish) appear larger in the latter part of the record (narrowband mode). The signal bandwidth also clearly affects the resolution of interface or turbulence imaging. Note also that apparent interfaces are thin early in the record while the ship is underway at approximately 7 knots, but are thicker later in the record when narrowband waveforms are used (and when the ship is not moving, making them appear relatively flat). There is a possibility that zooplankton are associated with the interfaces and that the physical structure is not being imaged, but at many time periods the volume scattering spectrum of thin echo layers (apparent interfaces) versus frequency, from 18 to 200 kHz, did not match the zooplankton spectral form which rises with frequency.

5.2. Diffusive–convective interface scattering

Fig. 10, showing one view of the intrusion that has been analyzed in detail, shows three sharp diffusive–convective interfaces passed through near times 18, 20 and 22 s, or order one-half meter apart. Here we use methods in a published study of backscattering from an interface of this type (Lavery and Ross, 2007) to evaluate the expected echo strength, and to see if it is consistent with the possible interface echoes in Fig. 12.

We make a prototype intrusion upper-side interface similar to those, subscripts 1 and 2 representing upper side and lower side conditions, respectively: $T_1 = 8.6$, $T_2 = 8.74$, $S_1 = 33.273$, $S_2 = 33.241$, pressure 46 dbar. For an incident plane wave, the scattering at the interface is independent of frequency and is given by $\psi = P_{\text{scat}}/P_{\text{inc}} = (\rho_2 c_2 - \rho_1 c_1)/(\rho_2 c_2 + \rho_1 c_1)$. For the prototype interface, $\psi = 2.7 \times 10^{-4}$, or -71 dB. Lavery and Ross (2007) show that interfering multiple closely spaced interfaces will reduce backscatter by 20–30 dB from this value. In this situation, the backscatter may be anywhere from -91 to -101 dB for interfaces that are coherent in structure over the span of a narrow acoustic beam (6 m for a 7-deg beam at 50 m).

On the other hand, Fig. 12 shows the returns to be in the -75 dB range, suggesting that single interfaces with no destructive interferences occur at least some of the time. Fig. 13 shows the echo expected from diffusive–convective interfaces over a range of temperature and salinity discontinuities. Interfaces with temperature steps above 0.07 °C are expected to produce returns above -85 dB and should be visible, as suggested by Fig. 12.

6. Conclusions

Data have been presented showing the nearby co-existence of DDI-diffusive/convective activity and DDI-finger activity in an intrusion with a remarkably stable core (Figs. 7 and 8). This demonstrates the small scales over which vastly different flow regimes and mixing regimes can exist in the ocean. These differences at very small scales may be important to tiny living organisms, for whom a meter may represent a thousand or more body lengths, and they are important for fully understanding mixing processes in the many ocean areas with fronts and measurable spiciness gradients. These examples of multiple processes within single intrusions point out the need to develop sampling tools and strategies to more fully examine mixing and dispersal of salt, heat, nutrients, plankton, and larvae in frontal regions.

Our computations suggest that acoustic systems may be usable only under conditions of low zooplankton activity, with this expectation supported by field data. The peak of DDI microstructure variance at wavelengths near 5 cm (Fig. 8), a larger scale than expected for vigorous turbulence, causes the backscatter signal from DDI processes to be less than that of energetic turbulence. The results show that rapidly sampling probes moving nearly horizontally may be put to good use measuring flow and instability behavior in acoustically mapped intrusions, perhaps coupled with tracer injections, although an ability to effectively guide sampling with acoustic remote sensing remains unproven.

There are good reasons to investigate intrusive (interleaving) process in detail. Errors may be introduced into computational flow models by parameterizing intermittent sub-grid scale process such as these observed DDI events as steady, as is typically done. In particular, thin layer activity and primary production patch activity would not be properly represented.

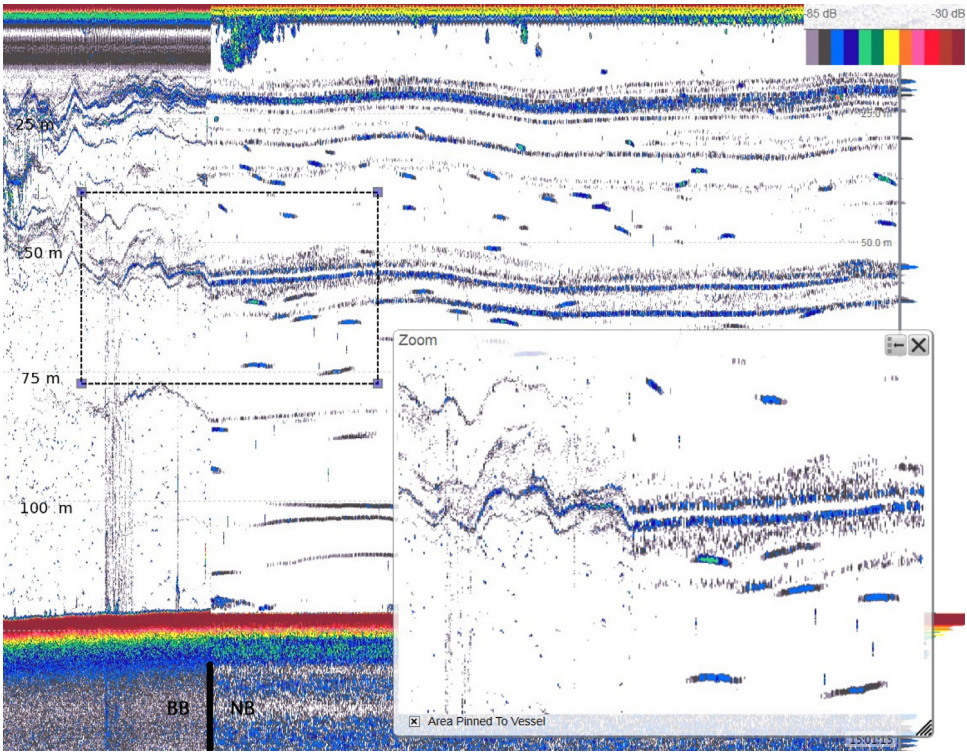

Fig. 12. A portion of a screen-grab from the Simrad EK80 echosounder control computer on the *RV Neil Armstrong* is shown. The 38-kHz channel is plotted. The end time is 20 June 2016 15:01:16 UTC, approx. 45 min of data are shown. Location at ending is 40–15.050N, 70–49.758W. Calibrated matched-filter output magnitudes are shown in dB. Gray and black are the weakest signals as indicated by the color scale; volume scattering levels below −85 dB are shown as white. The *y*-axis is gated recording time converted to depth, the *x*-axis is pulse index (clock time). The seabed is seen near 125 m depth. The zoom at the lower right shows the area outlined by the dashed box at its left. In the first portion of the record the ship is moving and this channel is operating in broadband mode. One-third of the way into the zoom period this channel is switched to narrowband mode (time indicated by black line in the seabed) for operation while the ship is on station; while the ship is on station the interface structure appears relatively flat and the transient reflectors (fish) appear long as they hover in the beam. (Broadband mode has finer vertical resolution.) Multiple detrimental interference and noise effects are visible in this section of data, in both modes. (For interpretation of the references to color in this figure legend, the reader is referred to the web version of this article.)

Finally, the measured small vertical scales of intrusions and the close vertical spacing of the intrusions may be valuable new information. A theoretical paper (May and Kelley, 1997) suggested that vertical wavelengths of interleaving should be on the order of 10 to 20 m, but that analysis imposed a background DDI-finger-favorable stratification not found in our area, so a regime in need of theoretical analysis may have been uncovered by these data.

Acknowledgments

The data were collected under Office of Naval Research grant N00014-03-1-0335. Acoustic analysis was done under grant N00014-14-1-0223/N00014-16-1-2372. The topside MT data collection and display software package was written by Ed Hobart. Chris Rehmann kindly provided data analysis codes. The MT data collection at sea was aided by the efforts of David Walsh and Nick Witzell. The efforts of the captain and crew of *RV Endeavor* are appreciated. The support of Chief Scientist Gareth Lawson, Peter Wiebe, Mike Jech, Jennifer Johnson and Dezhang Chu during *RV Neil Armstrong* acoustic testing is appreciated.

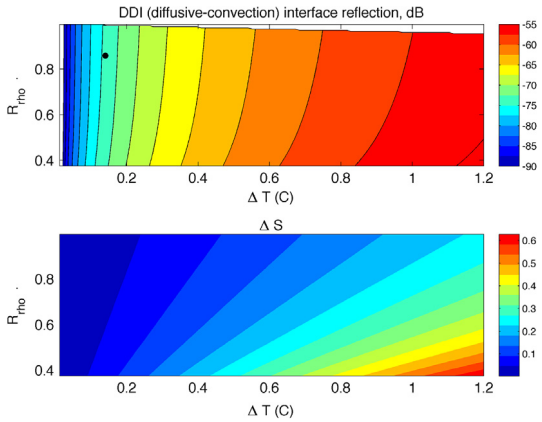

Fig. 13. (upper panel) The predicted reflection ψ from diffusive–convective type interfaces of varying temperature step (ΔT, °C) and density ratio (R_ρ) is contoured. The black dot marks the result for the upper side of the intrusion analyzed in the paper. ($\Delta T = 0.14$, $\Delta S = 0.032$ g/kg). (lower panel) The salinity step ΔS is contoured for the same ΔT and R_ρ ranges as the upper panel.

Appendix. Computation of acoustic backscatter cross-section

The acoustic backscatter is computed from the conductivity gradient spectrum as follows: First, a few parameters are defined. The acoustic frequency is f, $\omega = 2\pi f$, and the wavenumber is $k = \omega/c_0$ where c_0 is a reference sound speed (1500 m/s). The relationship of temperature and salinity in the background stratification is $m = dS/dT$.

The one-dimensional temperature spatial spectrum S_{TT} is computed from the one-dimensional (measured) conductivity gradient spectrum G_{CC} as follows, using a scaling factor s that accounts for the effects of correlated T and S gradients controlling conductivity gradients

$$S_{TT}(k) = \frac{sG_{CC}(k)}{2\pi k^2\left(A^2 + c_0^2\right)}.$$

The factor s can be approximated by analysis of figures in Washburn et al. (1996). The corresponding salinity spectrum is given by

$$S_{SS}(k) = m^2 S_{TT}(k).$$

The three-dimensional (3D) spectra of these quantities are given by

$$\Phi_N(k) = (2\pi k)^{-1}\, {}^{dS_{NN}}/_{dk}; \quad N = T, S.$$

For backscatter (angle between incident and scattered acoustic wavenumbers $\theta = \pi$), the Bragg wavenumber $K = 2k\sin(\theta/2) = 2k$. The backscatter cross-section per unit volume, computed from the 3D spectra, is given by Equation (20) of Lavery et al. (2003)

$$\sigma_V = 2\pi k^4\left(A^2\Phi_T(K) + B^2\Phi_S(K)\right).$$

Here, the cross-spectrum Φ_{ST} term of their Equation (20) is set to zero because it is not well known. The coefficients are $A = a - \alpha\sin 2(\theta/2)$, and $B = b + \beta\sin 2(\theta/2)$. Parameters used in the computation are given in Table 1.

References

Duda, T.F., Rehmann, C.R., 2002. Systematic microstructure variability in double-diffusively stable coastal waters of nonuniform density gradient. J. Geophys. Res. 107 (C10), 3144. http://dx.doi.org/10.1029/2001JC000844.

Duda, T.F., Sellers, C.J., 2016. Microscale, finescale, and mesoscale measurements made during the 2004 Structured Mixing Project (Micro-Tow 04) cruise, 2016. Woods Hole Oceanographic Institution Technical Report WHOI-2016-02.

Fer, I., Peterson, A.K., Ullgren, J.E., 2014. Microstructure measurements from an underwater glider in the turbulent Faroe bank channel overflow. J. Atmos. Ocean. Technol. 31, 1128–1150. http://dx.doi.org/10.1175/JTECH-D-13-00221.1.
Flament, P., 2002. A state variable for characterizing water masses and their diffusive stability: Spiciness. Prog. Oceanogr. 54, 493–501.
Gargett, A.E., Schmitt, R.W., 1982. Observations of salt fingers in the central waters of the eastern North Pacific. J. Geophys. Res. 87, 8017–8029.
Gregg, M.C., 1975. Microstructure and intrusions in the California current. J. Phys. Oceanogr. 5, 253–278.
Hill, K.D., Woods, D.J., 1988. The dynamic response of the two-electrode conductivity cell. IEEE J. Ocean. Eng. 13, 118–123.
Kelley, D.E., 1990. Fluxes through diffusive staircases: A new formulation. J. Geophys. Res. 95, 3365–3371.
Lavery, A.C., Chu, D., Moum, J., 2010. Observations of broadband acoustic backscattering from nonlinear internal waves: assessing the contribution from microstructure. IEEE J. Ocean. Eng. 34 (4), 695–709.
Lavery, A.C., Geyer, W.R., Scully, M.E., 2013. Broadband acoustic quantification of stratified turbulence. J. Acoust. Soc. Am. 134, 40–54.
Lavery, A.C., Ross, T., 2007. Acoustic scattering from double-diffusive microstructure. J. Acoust. Soc. Am. 122, 1449–1462.
Lavery, A.C., Schmitt, R.W., Stanton, T.K., 2003. High-frequency acoustic scattering from turbulent oceanic microstructure: The importance of density fluctuations. J. Acoust. Soc. Am. 114, 2685–2697.
Ledwell, J.R., Duda, T.F., Sundermeyer, M., Seim, H., 2004. Mixing in a coastal environment: 1. A view from dye dispersion. J. Geophys. Res. 109, C10013.
Lentz, S.J., 2003. A climatology of salty intrusions over the continental shelf from Georges bank to cape hatteras. J. Geophys. Res. 108 (C10), 3326. http://dx.doi.org/10.1029/2003JC001859.
Li, Y., McDougall, T.J., 2015. Double-diffusive interleaving: Properties of the steady-state solution. J. Phys. Oceanogr. 45, 813–835.
MacKinnon, J.A., Gregg, M.C., 2003. Mixing on the late-summer New England Shelf – Solibores, shear and stratification. J. Phys. Oceanogr. 33, 1476–1492.
Marmorino, G.O., 1987. Observations of small-scale mixing processes in the seasonal thermocline. Part I: Salt fingering. J. Phys. Oceanogr. 17, 1339–1347. http://dx.doi.org/10.1175/1520-0485(1987)017<1339:OOSSMP>2.0.CO;2.
May, B.D., Kelley, D.E., 1997. Effect of baroclinicity on double-diffusive interleaving. J. Phys. Oceanogr. 27, 1997–2008. http://dx.doi.org/10.1175/1520-0485(1997)027<1997:EOBODD>2.0.CO;2.
Meagher, T.B., Pederson, A.M., Gregg, M.C., 1982. A low noise conductivity microstructure instrument. In: Proc. Oceans'82. Mar. Technol. Soc. and IEEE Oceanic Engineering Society, New York, NY, pp. 283–290.
Oakey, N.S., Greenan, B.J.W., 2004. Mixing in a coastal environment: 2. A view from microstructure measurements. J. Geophys. Res. 109, C10014.
Orr, M.H., Mignerey, P.C., 2003. Nonlinear internal waves in the South China Sea: Observation of the conversion of depression internal waves to elevation internal waves. J. Geophys. Res. 108 (C3), 3064. http://dx.doi.org/10.1029/2001JC001163.
Osborn, T.R., 1988. Signatures of doubly diffusive convection and turbulence in an intrusive regime. J. Phys. Oceanogr. 18, 145–155.
Osborn, T.R., Lueck, R.G., 1985. Turbulence measurements with a submarine. J. Phys. Oceanogr. 15, 1502–1520. http://dx.doi.org/10.1175/1520-0485(1985)015<1502:TMWAS>2.0.CO;2.
Rehmann, C.R., Duda, T.F., 2000. Diapycnal diffusivity inferred from scalar microstructure measurements near the New England shelf/slope front. J. Phys. Oceanogr. 30, 1354–1371.
Ruddick, B., 1983. A practical indicator of the stability of the water column to double-diffusive activity. Deep-Sea. Res. 30, 1105–1107.
Schmitt, R.W., 1983. The characteristics of salt fingers in a variety of fluid systems, including stellar interiors, liquid metals, oceans, and magmas. Phys. Fluids 26, 2373–2377. http://dx.doi.org/10.1063/1.864419.
Schmitt, R.W., 1994. Double diffusion in oceanography. Annu. Rev. Fluid Mech. 26 (1), 255–285.
Schmitt, R.W., Evans, D.L., 1978. An estimate of the vertical mixing due to salt fingers based on observations in the North Atlantic central water. J. Geophys. Res. 83, 2913–2919.
Shcherbina, A.Y., Gregg, M.C., Alford, M.H., Harcourt, R.R., 2009. Characterizing thermohaline intrusions in the North Pacific subtropical frontal zone. J. Phys. Oceanogr. 39, 2735–2756.
Shcherbina, A.Y., Gregg, M.C., Alford, M.H., Harcourt, R.R., 2010. Three-dimensional structure and temporal evolution of submesoscale thermohaline intrusions in the North Pacific subtropical frontal zone. J. Phys. Oceanogr. 40, 1669–1689.
Timmermans, M.-L., Toole, J., Krishfield, R., Winsor, P., 2008. Ice-tethered profiler observations of the double-diffusive staircase in the Canada basin thermocline. J. Geophys. Res. 113, C00A02. http://dx.doi.org/10.1029/2008JC004829.
Turner, J.S., 1973. Buoyancy Effects in Fluids. Cambridge U. Press, Cambridge.
Walsh, D., Ruddick, B., 1998. Nonlinear equilibration of thermohaline intrusions. J. Phys. Oceanogr. 28, 1043–1070.
Washburn, L., Deaton, T.K., 1986. A simple system for mapping conductivity microstructure. J. Atmos. Ocean. Technol. 3, 345–355.
Washburn, L., Duda, T.F., Jacobs, D.C., 1996. Interpreting conductivity microstructure: Estimating the temperature variance dissipation rate. J. Atmos. Ocean. Technol. 13, 1166–1188.
Washburn, L., Gibson, C.H., 1982. Measurements of oceanic temperature microstructure using a small conductivity sensor. J. Geophys. Res. 87 (C6), 4230–4240. http://dx.doi.org/10.1029/JC087iC06p04230.